Interatomic potentials for monoatomic metals from experimental data and *ab initio* calculations

Y. Mishin and D. Farkas
Department of Materials Science and Engineering, Virginia Polytechnic Institute and State University, Blacksburg, Virginia 24061-0237

M. J. Mehl and D. A. Papaconstantopoulos
Complex Systems Theory Branch, Naval Research Laboratory, Washington, D.C. 20375-5345

(Received 19 November 1997; revised manuscript received 26 August 1998)

We demonstrate an approach to the development of many-body interatomic potentials for monoatomic metals with improved accuracy and reliability. The functional form of the potentials is that of the embedded-atom method, but the interesting features are as follows: (1) The database used for the development of a potential includes both experimental data and a large set of energies of different alternative crystalline structures of the material generated by *ab initio* calculations. We introduce a rescaling of interatomic distances in an attempt to improve the compatibility between experimental and *ab initio* data. (2) The optimum parametrization of the potential for the given database is obtained by alternating the fitting and testing steps. The testing step includes a comparison between the *ab initio* structural energies and those predicted by the potential. This strategy allows us to achieve the best accuracy of fitting within the intrinsic limitations of the potential model. Using this approach we develop reliable interatomic potentials for Al and Ni. The potentials accurately reproduce basic equilibrium properties of these metals, the elastic constants, the phonon-dispersion curves, the vacancy formation and migration energies, the stacking fault energies, and the surface energies. They also predict the right relative stability of different alternative structures with coordination numbers ranging from 12 to 4. The potentials are expected to be easily transferable to different local environments encountered in atomistic simulations of lattice defects. [S0163-1829(99)05005-5]

I. INTRODUCTION

In spite of greatly increased computer speeds, the application of *ab initio* methods for an atomistic simulation of materials is still limited to relatively small ensembles of atoms and, in molecular dynamics, relatively short simulation times. In contrast, the use of empirical or semiempirical interatomic potentials makes it possible to simulate much larger systems (up to 10^7-10^8 atoms) for much longer times, and thus to tackle such problems as plastic deformation, fracture, or atomic diffusion. For this reason there is and will probably always be a demand for realistic interatomic potentials, as there will always be a tendency to simulate as large systems as possible.

In this paper we propose an approach to the development of reliable interatomic potentials for monoatomic metals based on a large set of experimental and *ab initio* data. As an application we develop accurate many-body potentials for Al and Ni, which are intended for atomistic simulations of internal defects in these metals, such as point defects, planar faults, grain boundaries, and dislocations. The potentials can also be used for fracture simulations and, with some caution, simulations of surface phenomena. The choice of Al and Ni is dictated by the desire to test our approach for both simple (Al) and transition (Ni) metals. Furthermore, this work is a part of our current effort to develop reliable interatomic potentials for ordered intermetallic compounds of the Ni-Al system. The present potentials for Al and Ni will be incorporated into the potentials for the compounds.

In Sec. II of the paper we introduce our general approach to the development of interatomic potentials. We discuss the advantages and problems associated with using both experimental data and *ab initio* structural energies in one database. We also introduce a strategy of parametrization and optimization of interatomic potentials based on the separation of the fitting and testing steps. Section III describes our database and further details of the parametrization, fitting, and testing procedures. In Sec. IV we present the results of fitting and testing the potentials for Al and Ni. In Sec. V we summarize our results and discuss possible applications of the potentials.

II. GENERAL APPROACH

The potentials developed in this work are based on the formalism of the embedded-atom method (EAM).[1,2] In this method the total energy of a monoatomic system is represented as

$$E_{\mathrm{tot}}=\tfrac{1}{2}\sum_{ij} V(r_{ij})+\sum_i F(\overline{\rho}_i). \tag{1}$$

Here $V(r_{ij})$ is a pair potential as a function of the distance r_{ij} between atoms i and j, and F is the ''embedding energy'' as a function of the host ''density'' $\overline{\rho}_i$ induced at site i by all other atoms in the system. The latter is given by

$$\overline{\rho}_i=\sum_{j\neq i} \rho(r_{ij}), \tag{2}$$

$\rho(r_{ij})$ being the ''atomic density'' function. The second term in Eq. (1) is volume dependent and represents, in an approximate manner, many-body interactions in the system. EAM potentials, together with some other similar potentials,[3,4] are often referred to collectively as ''glue model'' potentials. All

glue model potentials share the same general form given by Eqs. (1) and (2), and only differ in the functional forms of $V(r)$, $\rho(r)$, and $F(\overline{\rho})$. In this work we use very general forms of the potential functions with no reference to their original physical meaning. Thus, while we often use the terminology of the EAM, our potentials could as well be classified as glue model potentials.

Once the general form of the potential is chosen, the important issues become how to choose the database for fitting and how to parametrize and optimize the potential functions. We shall discuss these issues in order.

A. Importance of *ab initio* data in the development of interatomic potentials

Empirical potentials for monoatomic metals are typically fitted to the experimental values of the equilibrium lattice parameter a_0, the cohesive energy E_0, three elastic constants, and the vacancy formation energy E_v^f. (For a noncubic material this data set includes additional elastic constants and the equilibrium c/a ratio.) This basic set of properties is often complemented with planar fault energies, low-index surface energies, phonon frequencies, and/or other data. Unfortunately, reliable experimental information on metal properties that can be directly linked to atomic interactions is very limited. Furthermore, most experimental properties represent the behavior of the material in very small regions of configuration space. For example, the elastic constants and phonon frequencies are determined by small atomic displacements from the equilibrium lattice configuration. In contrast, in atomistic simulations the system is free to explore different atomic configurations that can be quite far away from the regions represented by the experimental data. The question which then arises is the following: How accurately will the potential represent the energies of such ''abnormal'' configurations? The accuracy of the potential over a range of configurations, i.e., its *transferability*, obviously depends on whether the data points used for fitting span a wide enough region of configuration space.

A possible way to expand the database is to include a set of atomic configurations calculated by *ab initio* methods. For example, Ercolessi and Adams[5] recently proposed developing glue model potentials by fitting to both experimental data and *ab initio* atomic forces calculated for a large set of configurations including crystals, liquids, surfaces, and isolated clusters (force-matching method). Another possibility of incorporating *ab initio* data is to calculate a set of *structural energies*, i.e., energies of various crystalline structures of the same material with different lattice parameters. Such a set may include not only three-dimensional crystals but also slabs, layers, or even atomic chains.[6,7] In either case the incorporation of *ab initio* data can improve the accuracy and transferability of the potential dramatically by sampling regions of configuration space that are not accessible experimentally.

This recently emerged approach is very promising, and may serve to bridge the existing gap between *ab initio* and empirical methods in materials simulations. It should be mentioned, however, that the simultaneous use of experimental and *ab initio* data in one database entails some problems. In particular, many *ab initio* methods tend to underestimate the equilibrium lattice parameters of crystals in comparison with experimental data. This tendency to underestimate interatomic distances introduces some degree of incompatibility between the *ab initio* structural energies and the experimental quantities, and makes one-to-one fitting to the structural energies problematic. This applies equally to the force-matching method[5] where, again, the *ab initio* forces can be affected by the previous tendency. In the present paper we shall address this problem by introducing a rescaling of interatomic distances during the fitting and testing of the potentials.

B. Optimization of the fitting procedure

In some earlier studies the parametrization of the potential functions was based on simple functional forms reflecting, to some extent, their original physical meaning.[2,8,9] For example, $V(r)$ was represented by a Morse function and $\rho(r)$ by a combination of power and exponential functions. An alternative approach, taken in the glue model[3–5] and followed in this work, is to use a basis set of cubic splines which, although having no physical foundation, offer plenty of parameters for fitting.

For the development of an accurate potential it is important to have an *optimum* number of fitting parameters for the chosen database. While the lack of fitting parameters, and thus flexibility, may affect the accuracy of the potential, it is not good to have too many fitting parameters either.[6,10] As with any model potential, the general form of Eqs. (1) and (2) has certain physical limitations which cannot be overcome by including more parameters. Of course, having a sufficient number of parameters, one can fit all points in the data set exactly, but the potential thus obtained will perform badly on configurations other than those represented by the data set. Robertson, Heine, and Payne[6] recently proposed a strategy which avoids the overfitting of the database. They suggested splitting the database into two parts and using one part for fitting and the other for testing the potential. If the root-mean-square (rms) deviation between the desired and predicted properties observed at the testing stage is considerably larger than the rms deviation achieved at the fitting step, the database is probably overfitted and the number of parameters should be reduced. Robertson *et al.*[6] and Payne *et al.*[10] demonstrated that the rms deviation obtained while fitting gives no indication of the accuracy of the potential; instead, it is the rms deviation obtained at the testing stage that gives the most meaningful measure of the quality of the potential.

The separation of the fitting and testing steps suggests an algorithm for finding the optimum number of parameters. Thus one can start with a small number of fitting parameters and increase it gradually as long as both rms deviations decrease. Eventually, however, the rms deviation observed at the testing stage will stop decreasing and reach saturation, although the fitting rms deviation may continue to decrease. At this point the process can be stopped because the introduction of new parameters will not lead to any further improvement of the potential. The occurrence of saturation indicates that we have approached the limit of accuracy dictated by the intrinsic shortcomings of the adopted potential model. Robertson, Heine, and Payne[6] illustrated this strategy by fitting different glue model potentials for Al to a

large set of structural energies generated by *ab initio* pseudopotential calculations. In the present work we apply a similar strategy to establish the optimum number of fitting parameters for our database.

III. PARAMETRIZATION AND FITTING PROCEDURES

A. Database for fitting and testing

1. Experimental data

The experimental part of our database includes the following physical properties of Al and Ni: the equilibrium lattice parameter,[11] the cohesive energy,[12,13] the elastic constants c_{11}, c_{12}, and c_{44},[14] and the vacancy formation energy[15,16] (see Tables I and II). These experimental values coincide with those employed by Voter and Chen[9] in the development of their EAM potentials for these elements. The potentials of Voter and Chen, which we refer to hereafter as VC potentials, have been widely used in atomistic simulations, although other EAM potentials for Al and Ni are also available (see, e.g., Refs. 8 and 17–27). We use the VC potentials as a reference for comparison with our potentials throughout the paper. It should be mentioned that the VC potentials were obtained as a part of the development of EAM potentials for $L1_2$ Ni_3Al, and were later incorporated in EAM potentials for $B2$ NiAl.[28–30] We can thus conveniently extend the comparison with VC potentials to our current work on Ni-Al intermetallics.

Additionally, our database includes the experimental values of the vacancy migration energy E_v^m,[16,31] the intrinsic stacking fault energy γ_{SF},[32] and the experimentally measured phonon-dispersion relations.[33–35] The saddle-point configuration arising during a vacancy jump represents an important region of configuration space which is not represented by any other properties. The local density at the jumping atom in the saddle-point configuration is usually lower than that at a regular lattice atom, while the distances to the nearest neighbors are considerably smaller.[36] Therefore the energy of this configuration, and thus E_v^m, measure the strength of pairwise repulsion between atoms at short distances. The atomic interaction in this regime is not fitted properly in the traditional EAM scheme, with the consequence that EAM potentials typically underestimate E_v^m.[30] γ_{SF} represents the relative stability of the hcp phase, and determines the width of the dislocation dissociation on the (111) plane. Realistic values of γ_{SF} are thus critically important in simulations of plastic deformation and fracture. The agreement with experimental phonon frequencies is also essential, and, moreover, is considered as a criterion of global reliability of an empirical potential.[37]

Two more experimental properties included in the database were the surface energy γ_s and the equation of state (EOS), i.e., the crystal energy as a function of the lattice parameter a. We did not fit the potentials exactly to the energies of low-index planes (100), (110), and (111) because their experimental values are not very reliable. Instead, we only required that $\gamma_s(110) > \gamma_s(100) > \gamma_s(111)$, and that all three energies be close to the surface energy of an ''average'' orientation [980 mJ/m^2 for Al and 2280 mJ/m^2 for Ni (Refs. 32 and 38)]. The EOS was taken in the form of the universal empirical EOS of Rose *et al.*,[39] which uses only a_0, E_0, and the bulk modulus $B=(c_{11}+2c_{12})/3$ as physical parameters.

2. Ab initio data

Ab initio structural energies were generated using the first-principles linearized augmented plane-wave (LAPW) method,[40,41] including all electrons and allowing for a general potential. The electronic exchange and correlation was specified by the Perdew-Wang parametrization[42] of the local-spin-density (LSD) approximation within the Kohn-Sham formulation of density-functional theory.[43] Brillouin-zone integrations were performed using the ''special'' **k**-point set of Monkhorst and Pack,[44] modified[45] to sample correctly the Brillouin zone of lower-symmetry lattices. To speed convergence, we follow Gillan[46] and smear out the electronic eigenvalues with a Fermi distribution at $T=2$ m Ry. We use a rather large basis set and **k**-point mesh, so that energies are converged to better than 0.5 m Ry/atom. Aluminum-only calculations were carried out in spin-restricted mode, allowing no magnetic moment. Calculations involving Ni were carried out using the spin-polarized LSD by artificially inducing a magnetic moment on the nickel ions in the starting charge density and iterating to self-consistency. The comparison of the *ab initio* structural energies with those predicted by the EAM potential was performed as follows.

First, because the two types of calculation use different reference levels of energy, only energy differences between different structures could be compared with one another. In order to make this comparison more illustrative, we simply shifted all *ab initio* energies by the amount of $E_0-\tilde{E}_0$, where E_0 is the experimental cohesive energy of the fcc phase and $\tilde{E}_0$ is the *ab initio* energy per atom of an equilibrium fcc crystal. Due to this shift the *ab initio* calculations predict the right cohesive energy of the fcc phase by definition. If $\tilde{E}(R)$ is the *ab initio* energy per atom of any other crystalline structure with a first-neighbor distance R, then it is the quantity $E_0-\tilde{E}_0+\tilde{E}(R)$ that should be compared with the respective structural energy $E(R)$ predicted by the EAM potential:

$$E(R)\sim E_0-\tilde{E}_0+\tilde{E}(R). \tag{3}$$

Second, because of the LSD approximation our LAPW calculations tend to underestimate the interatomic distances in the crystal energy versus R dependence. This tendency manifests itself, in particular, in the underestimation of the equilibrium lattice parameter. Thus, for fcc Al and Ni our LAPW calculations predict $a_0=3.988$ and 3.428 Å, respectively (using the approximation by Birch's[47] EOS). Both values are on the lower side of the experimental lattice parameters $a_0=4.050$ and 3.520 Å, respectively. The ratio α of the respective lattice parameters, or the equilibrium first-neighbor distances $R_0=a_0/\sqrt{2}$, equals $\alpha=0.985$ for Al and 0.974 for Ni.

This difference in interatomic distances makes one-to-one comparison of *ab initio* and EAM-predicted structural energies, as suggested by Eq. (3), essentially inaccurate. In particular, for an equilibrium fcc crystal ($R=R_0$) we have the true cohesive energy E_0 in the left-hand side of Eq. (3) (because the EAM potential is fit exactly to E_0; see below) and

TABLE I. Properties of Al predicted by EAM potentials in comparison with experimental and *ab initio* data. *Fitted with high weight.† Fitted with low weight.

	Experiment or *ab initio*	Present work	Voter and Chen (Ref. 9)
Lattice properties:			
a_0 (Å)*	4.05[a]	4.05	4.05
E_0 (eV/atom)*	−3.36[b]	−3.36	−3.36
B (10^{11} Pa)*	0.79[c]	0.79	0.79
c_{11} (10^{11} Pa)*	1.14[c]	1.14	1.07
c_{12} (10^{11} Pa)*	0.619[c]	0.616	0.652
c_{44} (10^{11} Pa)*	0.316[c]	0.316	0.322
Phonon frequencies:			
$\nu_L(X)$ (THz)†	9.69[d]	9.31	8.55
$\nu_T(X)$ (THz)†	5.80[d]	5.98	5.20
$\nu_L(L)$ (THz)	9.69[d]	9.64	8.86
$\nu_T(L)$ (THz)	4.19[d]	4.30	3.70
$\nu_L(K)$ (THz)	7.59[d]	7.30	6.87
$\nu_{T_1}(K)$ (THz)	5.64[d]	5.42	4.80
$\nu_{T_2}(K)$ (THz)	8.65[d]	8.28	7.76
Other structures:			
E(hcp) (eV/atom)*	−3.33[e]	−3.33	−3.34
E(bcc) (eV/atom)*	−3.25[e]	−3.24	−3.28
E(diamond) (eV/atom)†	−2.36[e]	−2.33	−2.06
Vacancy:			
E_v^f (eV)*	0.68[f]	0.68	0.63
E_v^m (eV)*	0.65[g]	0.64	0.30
Interstitial:			
$E_I^f(O_h)$ (eV)		2.79	2.10
E_I^f ([111]-dumbbell) (eV)		3.00	2.51
E_I^f ([110]-dumbbell) (eV)		2.91	2.24
E_I^f ([100]-dumbbell) (eV)		2.59	2.06
Planar defects:			
γ_{SF} (mJ/m^2)*	166[h], 120–144[i]	146	76
γ_{us} (mJ/m^2)		168	93
γ_T (mJ/m^2)	75[h]	76	42
$\gamma_{gb}(210)$ (mJ/m^2)		495	366
$\gamma_{gb}(310)$ (mJ/m^2)		467	320
Surfaces:			
$\gamma_s(110)$ (mJ/m^2)†	980[j]	1006	959
$\gamma_s(100)$ (mJ/m^2)†	980[j]	943	855
$\gamma_s(111)$ (mJ/m^2)†	980[j]	870	823

[a]Reference 11.
[b]Reference 12.
[c]Reference 14.
[d]Reference 33. The results in tabulated form can be found in Ref. 35.
[e]Calculated in this work assuming the same nearest-neighbor distance as in the equilibrium fcc phase.
[f]Reference 15.
[g]Reference 31.
[h]Reference 32.
[i]References 51, 52.
[j]For average orientation, Ref. 32. Other estimates give 1140 mJ/m^2 (Ref. 38).

TABLE II. Properties of Ni predicted by EAM potentials in comparison with experimental and *ab initio* data. *Fitted with high weight. †Fitted with low weight.

	Experiment or *ab initio*	Present work	Voter and Chen (Ref. 9)
Lattice properties:			
a_0 (Å)*	3.52[a]	3.52	3.52
E_0 (eV/atom)*	−4.45[b]	−4.45	−4.45
B (10^{11} Pa)*	1.81[c]	1.81	1.81
c_{11} (10^{11} Pa)*	2.47[c]	2.47	2.44
c_{12} (10^{11} Pa)*	1.47[c]	1.48	1.49
c_{44} (10^{11} Pa)*	1.25[c]	1.25	1.26
Phonon frequencies:			
$\nu_L(X)$ (THz)†	8.55[d]	8.71	10.03
$\nu_T(X)$ (THz)†	6.27[d]	6.38	6.68
$\nu_L(L)$ (THz)	8.88[d]	8.53	10.04
$\nu_T(L)$ (THz)	4.24[d]	4.31	4.37
$\nu_L(K)$ (THz)	7.30[d]	6.98	8.08
$\nu_{T_1}(K)$ (THz)	5.78[d]	5.68	6.04
$\nu_{T_2}(K)$ (THz)	7.93[d]	8.04	9.23
Other structures:			
E(hcp) (eV/atom)*	−4.42[e]	−4.43	−4.44
E(bcc) (eV/atom)*	−4.30[e]	−4.30	−4.35
E(diamond) (eV/atom)†	−2.51[e]	−2.50	−2.61
Vacancy:			
E_v^f (eV)*	1.60[f]	1.60	1.56
E_v^m (eV)*	1.30[f]	1.29	0.98
Interstitial:			
$E_I^f(O_h)$ (eV)		5.86	4.91
E_I^f ([111]-dumbbell) (eV)		5.23	5.37
E_I^f ([110]-dumbbell) (eV)		5.80	5.03
E_I^f ([100]-dumbbell) (eV)		4.91	4.64
Planar defects:			
γ_{SF} (mJ/m^2)*	125[g]	125	58
γ_{us} (mJ/m^2)		366	225
γ_T (mJ/m^2)	43[g]	63	30
$\gamma_{gb}(210)$ (mJ/m^2)		1572	1282
$\gamma_{gb}(310)$ (mJ/m^2)		1469	1222
Surfaces:			
$\gamma_s(110)$ (mJ/m^2)†	2280[h]	2049	1977
$\gamma_s(100)$ (mJ/m^2)†	2280[h]	1878	1754
$\gamma_s(111)$ (mJ/m^2)†	2280[h]	1629	1621

[a]Reference 11.
[b]Reference 13.
[c]Reference 14.
[d]Reference 34.
[e]Calculated in this work assuming the same nearest-neighbor distance as in the equilibrium fcc phase.
[f]Reference 16.
[g]Reference 32.
[h]For average orientation, see Refs. 32 and 38.

the energy of a uniformly expanded crystal on the right-hand side. (For example, for Ni the excess energy associated with this expansion is about 0.04 eV/atom, which is larger than the energy difference between the fcc and hcp phases.) In order to remove this inconsistency in a first approximation, we modified Eq. (3) by rescaling all distances in the right-hand side by a factor of α:

$$E(R) \sim E_0 - \tilde{E}_0 + \tilde{E}(\alpha R). \tag{4}$$

This relation becomes an identity when applied to the equilibrium fcc phase, and is expected to be more accurate than Eq. (3) when applied to other structures and R values. Although based on heuristic arguments rather than solid physical grounds, this rescaling offers a first step in improving the one-to-one comparison scheme [Eq. (3)] used in previous studies.[5–7]

It should be mentioned that the rescaling of interatomic distances can influence some properties of the material predicted by *ab initio* calculations, in particular the elastic constants. It was therefore interesting to evaluate how the rescaling changes such properties in comparison with experimental data. In cases where this comparison was possible, the effect of the rescaling was either insignificant or favorable. For example, the elastic constants for Al predicted by our LAPW calculations are $c_{11}=128\pm 8$, $c_{12}=64\pm 5$, and $c_{44}=39\pm 5$ GPa. These values are systematically higher than the experimental values listed in Table I. Because the elastic constants are proportional to the second spatial derivatives of energy, the rescaling according to Eq. (4) results in multiplying them by factor α^2. This slightly reduces the elastic constants ($c_{11}=124$, $c_{12}=62$, and $c_{44}=38$ GPa), and makes them closer to the experimental values. Although the effect is not very large, it can be taken as confirmation of the reasonable character of Eq. (4).

In accordance with Eq. (4), we used two type of structural energies for fitting to or testing against each other: (1) *Ab initio* energies for a set of different structures with a fixed first-neighbor distance R, which constitutes a certain fraction f of the *ab initio* value of R_0. (2) EAM-predicted energies for the same set of structures with a fixed R equal to the same fraction f of the experimental value of R_0. Our *ab initio* data set included the fcc, hcp, bcc, simple hexagonal (sh), simple cubic (sc), $L1_2$ (fcc with one vacancy per simple cubic unit cell), and diamond structures. The hexagonal structural energies were taken with the ideal c/a ratio. For Al we also included the $\beta-W$ (A15) structure, and for Ni this structure was not calculated because of computational limitations. The energy of each structure was calculated with three values of R: $0.95R_0$, R_0, and $1.1R_0$.

B. Parametrization of potential functions

Functions $V(r)$ and $\rho(r)$ were represented as

$$V(r) = V_s(r) - V_s'(r_c)\psi(r-r_c), \tag{5}$$

$$\rho(r) = \rho_s(r) - \rho_s'(r_c)\psi(r-r_c). \tag{6}$$

Here r_c is a common cutoff radius of both functions, and $\psi(x)=x/(1+\beta^n x^n)$ is a cutoff function which serves to guarantee that both the first and second derivatives of $V(r)$ and $\rho(r)$ tend to zero as $r\to r_c$. In this work we chose $\beta=2$ Å^{-1} and $n=4$, while r_c was treated as a fitting parameter. Functions $V_s(r)$ and $\rho_s(r)$ in Eqs. (5) and (6) are cubic splines through given sets of points $\{r_i, V_i\}$ $(i=1,...,N_1)$ and $\{r_i,\rho_i\}$ $(i=1,\ldots,N_2)$ with natural boundary conditions. The last point in each set is, of course, $(r_c,0)$. The two functions $V(r)$ and $\rho(r)$ are thus parametrized by a total of N_1+N_2-1 parameters, namely, $\{V_i\}$ $(i=1,\ldots,N_1-1)$, $\{\rho_i\}$ $(i=1,\ldots,N_2-1)$, and r_c.

Likewise, the embedding function $F(\overline{\rho})$ was represented by a cubic spline through a set of points $\{\overline{\rho}_i, F_i\}$ $(i=1,\ldots,N_3)$. This set includes the points (0,0) and $(\overline{\rho}_0, F_0)$, where $\overline{\rho}_0$ is the density corresponding to the equilibrium fcc crystal and $F_0 \equiv F(\overline{\rho}_0)$ is the equilibrium embedding energy. Given the functions $V(r)$ and $\rho(r)$, the values of $\overline{\rho}_0$ and F_0, as well as the derivatives F_0' and F_0'' at equilibrium, can be determined uniquely from the experimental values of a_0, E_0, and B. Indeed, considering the crystal energy per atom, E, and introducing the summation over coordination shells within the cutoff sphere, Eqs. (1) and (2) give

$$\overline{\rho}_0 = \sum_m N_m \rho_m, \tag{7}$$

$$F_0 = E_0 - \tfrac{1}{2}\sum_m N_m V_m. \tag{8}$$

Here $V_m \equiv V(R_m)$, $\rho_m \equiv \rho(R_m)$, R_m is the radius of the mth coordination shell at equilibrium, and N_m is the number of atoms at the mth coordination shell. Furthermore, by calculating the first and second derivatives of E with respect to the first-neighbor distance, we obtain, respectively,

$$\tfrac{1}{2}\sum_m N_m V_m' R_m + F_0' \sum_m N_m \rho_m' R_m = 0, \tag{9}$$

$$\tfrac{1}{2}\sum_m N_m V_m'' R_m^2 + F_0' \sum_m N_m \rho_m'' R_m^2 + F_0''\left(\sum_m N_m \rho_m' R_m\right)^2 = 9B\Omega_0, \tag{10}$$

Ω_0 being the equilibrium atomic volume, V_m', V_m'', ρ_m', and ρ_m'' the respective derivatives of the functions at coordination shells. Equation (9) expresses the condition of mechanical equilibrium of the crystal, while Eq. (10) relates the second derivative of E to the bulk modulus B. We can thus determine F_0, F_0', and F_0'' from Eqs. (8), (9), and (10), respectively. Given these values, point $(\overline{\rho}_0, F_0)$ of the spline turns out to be fixed, while F_0' and F_0'' uniquely determine the boundary conditions of the spline. The number of fitting parameters associated with the embedding function is therefore N_3-2. Note that this scheme of parametrization provides an exact fit of the potential to a_0, E_0, and B.

The basic equations (1) and (2) are known to be invariant under the transformations

$$\rho(r) \to s\rho(r), \quad F(\overline{\rho}) \to F(\overline{\rho}/s) \tag{11}$$

and

$$F(\overline{\rho}) \to F(\overline{\rho}) - g\overline{\rho}, \quad V(r) \to V(r) + 2g\rho(r), \qquad (12)$$

where s and g are arbitrary constants. Of special interest is the choice of $g = F_0'$, called the effective pair scheme;[48] in this case $F(\overline{\rho})$ has a minimum at $\overline{\rho}_0$, which greatly simplifies all expressions for the elastic moduli and lattice force constants. In any case the invariance of the EAM model, expressed by Eqs. (11) and (12), reduces the number of free fitting parameters by two. This reduction can be implemented by fixing one node point in each of the spline functions $V_s(r)$ and $\rho_s(r)$ at some arbitrary values. Thus the total number of free fitting parameters in our parametrization scheme equals $N_p = N_1 + N_2 + N_3 - 5$.

C. Fitting procedure

We used a computer code designed for fitting the potential functions to a_0, E_0, B, c_{11}, and c_{12}; phonon frequencies at the zone edge point X; unrelaxed values of E_v^f, E_v^m, $\gamma_{\rm SF}$, $\gamma_s(100)$, $\gamma_s(110)$, and $\gamma_s(111)$; an empirical EOS for any given set of lattice parameters; and the energies of several alternative structures with the same first-neighbor distance as that in the equilibrium fcc phase (R_0). In this work the potentials were fitted to the *ab initio* energies of the hcp, bcc, and diamond structures using Eq. (4) for comparison; all other structural energies were left for the testing stage.

As mentioned above, our parametrization scheme guarantees an exact fit to a_0, E_0, and B. For all other properties we minimized the sum of relative squared deviations from the desired values with a certain weight assigned to each property. The minimization was performed using the simplex algorithm of Nelder and Mead[49] with many different starting conditions. The weights were used as a tool to control the priority of certain properties over others according to the reliability of the data points, the intended application of the potential, and the intrinsic shortcomings of the EAM model. Thus the highest priority was given to the elastic constants, E_v^f, E_v^m, and $\gamma_{\rm SF}$ and the energies of the hcp and bcc structures. The phonon frequencies, the energy of the diamond structure and especially the surface energies were included with the lowest weights. The diamond structure has the lowest coordination number ($z = 4$) and shows the largest deviation from the ground-state fcc structure in comparison with all other structures considered in this work. Although we did find it necessary to sample this region of configuration space, the diamond structure was assigned a low weight for two reasons: (1) Equation (4) is unlikely to be reliable at such extreme deviations from the fcc structure. (2) The occurrence of such low coordinations is less probable in simulations of internal defects in metals.

The empirical EOS of Rose *et al.*[39] was fitted at 24 lattice parameters in the range from $0.8a_0$ to $1.4a_0$, but again with a relatively small weight. We did not expect this universal EOS to be very accurate when applied to the specific metals in study, particularly far from equilibrium. However, the exclusion of the empirical EOS from the data set resulted in drastic overfitting of the database, and the EOS predicted by the potential attained additional inflection points or even local minima. It was therefore helpful to keep the empirical EOS in the database, even though with a small weight, so as to avoid the overfitting and suppress the unphysical features in the predicted EOS.

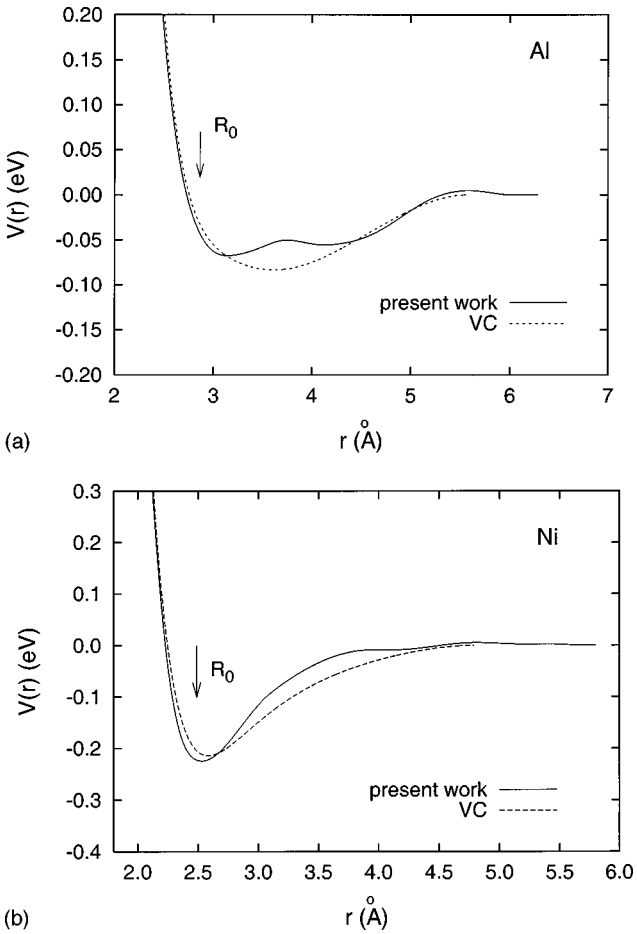

FIG. 1. EAM potentials for Al (a) and Ni (b) in the effective pair format.

Because the program operated only with unrelaxed quantities, the fitting to the relaxed values of E_v^f, E_v^m, and $\gamma_{\rm SF}$ was performed by trial and error. In this procedure one gains a good feeling for the relaxation energies after just a few trials, and can achieve fairly good accuracy of fitting in a reasonable number of iterations.

The optimum number of fitting parameters for our database was established by alternating fitting and testing as discussed in Sec. II. To implement this strategy we had to generate a large set of potentials with different numbers (N_p) of fitting parameters. Each potential was tested for the rms deviation between EAM-predicted and *ab initio* values of the structural energies other than those included in the fitting database. While the rms deviation of fitting decreased with N_p, the rms deviation observed at the testing stage first decreased, then reached a saturation, and finally increased. The potential corresponding approximately to the onset of the saturation was identified as the optimum potential.

IV. INTERATOMIC POTENTIALS FOR Al AND Ni

The optimum potentials were found to be those with $N_1 = 9$, $N_2 = 7$, and $N_3 = 6$ (thus $N_p = 17$) for Al, and $N_1 = 9$, $N_2 = 7$, and $N_3 = 5$ (thus $N_p = 16$) for Ni. They are shown in the effective pair format in Fig. 1. In this format both potentials have two local minima and are, in this respect, similar to the Al potential of Ercolessi and Adams.[5] The cutoff radii are

TABLE III. Tabulated potential functions for Al and Ni. See Eq. (1) in the text for notation.

Al			Ni			Al		Ni	
r (Å)	V (eV)	ρ	r (Å)	V (eV)	ρ	$\bar{\rho}$	F (eV)	$\bar{\rho}$	F (eV)
2.000	1.3467	0.0808	2.0000	0.7597	0.0671	0.000	0.0000	0.0000	0.0000
2.1786	0.8365	0.0835	2.1585	0.1812	0.0727	0.050	−0.6192	0.050	−0.2164
2.3573	0.4096	0.0852	2.3170	−0.1391	0.0761	0.100	−1.0792	0.100	−0.5094
2.5359	0.1386	0.0847	2.4755	−0.2214	0.0755	0.150	−1.4100	0.150	−0.8488
2.7145	0.0062	0.0808	2.6340	−0.2153	0.0691	0.200	−1.6414	0.200	−1.2042
2.8932	−0.0488	0.0724	2.7924	−0.1766	0.0579	0.250	−1.8033	0.250	−1.5453
3.0718	−0.0665	0.0602	2.9509	−0.1291	0.0440	0.300	−1.9255	0.300	−1.8419
3.2504	−0.0662	0.0463	3.1094	−0.0909	0.0301	0.350	−2.0330	0.350	−2.0714
3.4291	−0.0605	0.0328	3.2679	−0.0643	0.0193	0.400	−2.1313	0.400	−2.2426
3.6077	−0.0529	0.0220	3.4264	−0.0423	0.0123	0.450	−2.2209	0.450	−2.3721
3.7863	−0.0503	0.0145	3.5849	−0.0252	0.0081	0.500	−2.3024	0.500	−2.4766
3.9650	−0.0537	0.0096	3.7434	−0.0139	0.0057	0.550	−2.3764	0.550	−2.5698
4.1436	−0.0554	0.0066	3.9019	−0.0089	0.0043	0.600	−2.4434	0.600	−2.6542
4.3222	−0.0535	0.0048	4.0604	−0.0084	0.0031	0.650	−2.5038	0.650	−2.7296
4.5009	−0.0485	0.0036	4.2189	−0.0078	0.0021	0.700	−2.5574	0.700	−2.7958
4.6795	−0.0400	0.0029	4.3773	−0.0043	0.0014	0.750	−2.6039	0.750	−2.8525
4.8581	−0.0279	0.0025	4.5358	0.0006	0.0008	0.800	−2.6428	0.800	−2.8995
5.0368	−0.0149	0.0022	4.6943	0.0044	0.0004	0.850	−2.6737	0.850	−2.9364
5.2154	−0.0041	0.0018	4.8528	0.0052	0.0002	0.900	−2.6963	0.900	−2.9631
5.3940	0.0025	0.0015	5.0113	0.0037	0.0001	0.950	−2.7101	0.950	−2.9793
5.5727	0.0048	0.0011	5.1698	0.0022	0.0000	0.975	−2.7136	0.975	−2.9834
5.7513	0.0034	0.0006	5.3283	0.0024	0.0000	1.000	−2.7148	1.000	−2.9848
5.9299	0.0006	0.0001	5.4868	0.0020	0.0000	1.025	−2.7137	1.025	−2.9840
6.1086	−0.0001	0.0000	5.6453	0.0004	0.0000	1.050	−2.7108	1.050	−2.9838
6.2872	0.0000	0.0000	5.8037	0.0000	0.0000	1.100	−2.7016	1.100	−2.9990

$r_c = 6.287$ Å for Al and 5.804 Å for Ni. While the VC potentials limit the interactions to three coordination shells, our potentials include also the fourth, and the potential for Ni even includes the fifth, coordination shell. The effective pair interaction with these coordination shells is repulsive and, of course, very weak. The obtained potential functions are tabulated in Table III with 25 points per function. By applying some interpolation between the tabulated points the reader can reproduce the functions and use them for approximate calculations. For more accurate calculations, like those reported in this paper, the potentials were tabulated with 3000 points per function and the intermediate values were determined by means of cubic-spline interpolation. These potential files are available via the World Wide Web[50] or via e-mail at mishin@vt.edu.

In Tables I and II we list the data included in the fitting databases in comparison with the values predicted by the potentials. It is observed that the experimental values of the equilibrium properties, elastic constants, vacancy formation, and migration energies, and stacking fault energies are reproduced perfectly. The right values of E_v^f and E_v^m are important for the simulation of diffusion kinetics, radiation damage, and similar phenomena. While for Ni most of the existing potentials predict reasonable values of both E_v^f and E_v^m, for Al the agreement is usually poorer, especially with respect to E_v^m. Taking the most recent Al potentials,[5,25] for example, the Ercolessi-Adams potential predicts $E_v^m = 0.61$ eV, in good agreement with the experimental data (0.65 eV), while the potential of Rohrer gives an underestimated value of $E_v^m = 0.481$ eV.

For Al, the earlier experimental value of $\gamma_{SF} = 166\ \mathrm{mJ/m^2}$ (Ref. 32) was later re-interpreted as about 120 $\mathrm{mJ/m^2}$ (Refs. 51 and 52); we thus chose to fit γ_{SF} to an intermediate value of 146 $\mathrm{mJ/m^2}$. For both Al and Ni, the experimental γ_{SF} values are significantly higher than those predicted by the VC potentials. It should be mentioned that some of the most recent potentials developed by other groups also predict rather high values of γ_{SF}, particularly 104 $\mathrm{mJ/m^2}$ (Ref. 5) and 126 $\mathrm{mJ/m^2}$ (Ref. 25) for Al.

To provide an additional confirmation that the higher γ_{SF} values represent the right trend, we have evaluated γ_{SF} in Al by *ab initio* calculations. We used a five-layer supercell which realized the stacking sequence

$$\ldots BCABC|BCABC|BCABC\ldots,$$

with stacking faults separated by just five (111) layers. The unrelaxed stacking fault energy deduced from such calculations was $136 \pm 16\ \mathrm{mJ/m^2}$, which is comparable with the value of 157 $\mathrm{mJ/m^2}$ obtained for the same supercell using our potential. In contrast, the VC potential predicts a relatively low γ_{SF} value of 87 $\mathrm{mJ/m^2}$ for this geometry.

An important success of our potentials is that they show good agreement with experimental phonon-dispersion curves (Fig. 2). Although only the phonon frequencies at point X were included in the fitting database, all other frequencies are also reproduced with fairly good accuracy. The somewhat larger discrepancy observed for Al may have two sources.

(1) Al is more difficult for the EAM model than many noble and transition metals. This may be due to the unusually high electron density and thus extreme importance of many-

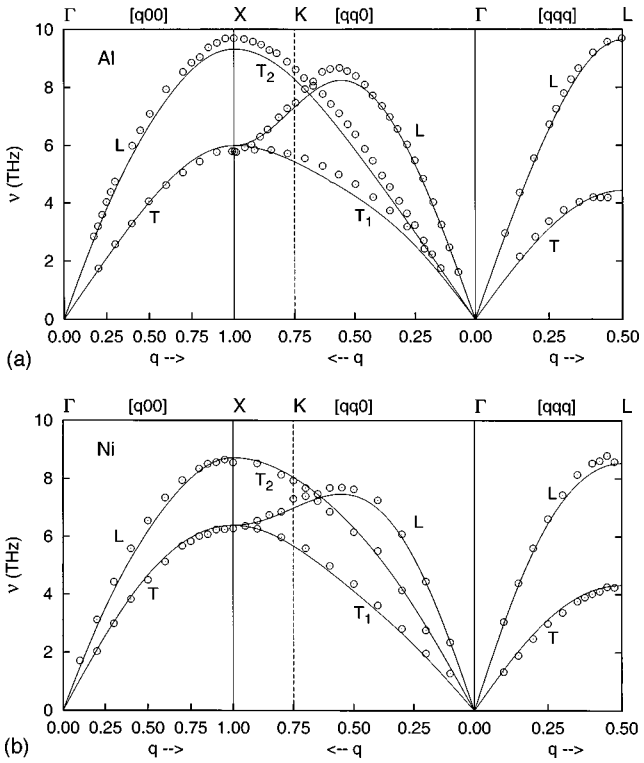

FIG. 2. Comparison of phonon-dispersion curves for Al (a) and Ni (b) predicted by the present EAM potentials, with the experimental values measured by neutron diffraction at 80 K (Al) and 298 K (Ni) (Ref. 33 for Al and Ref. 34 for Ni). The phonon frequencies at point X were included in the fitting database with low weight.

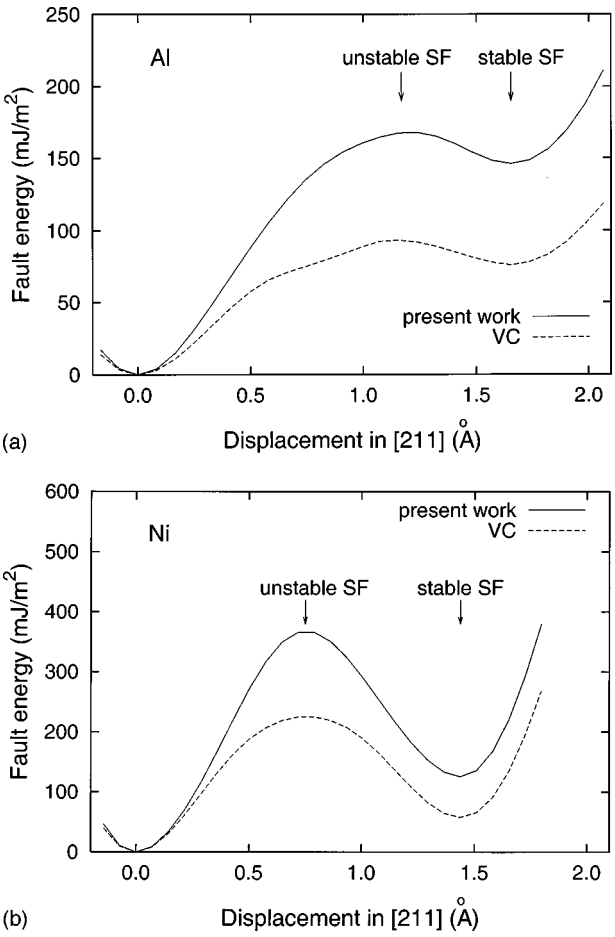

FIG. 3. Calculated sections of the γ surface of Al (a) and Ni (b) on (111) plane along [211] direction. The positions of the stable and unstable stacking faults are indicated.

body interactions, which are accounted for in the EAM model in an oversimplified manner.

(2) Some mismatch between the slopes of the experimental and calculated dispersion curves in the long-wavelength regions (especially for the transverse branches in $[qq0]$ direction; see Fig. 2(a)) indicates that there is some disagreement between the elastic constants that can be deduced from the experimental phonon-dispersion curves, on the one hand, and those obtained by ultrasonic measurements and used in our database, on the other hand.

The latter type of discrepancy has nothing in common with the intrinsic limitations of the EAM model. The Al potential of Ercolessi and Adams[5] also gives a good agreement with the experimental phonon frequencies. For all other Ni and Al potentials that could be tested in this work, the agreement was considerably poorer.

For self-interstitials, both our potentials and those of Voter and Chen predict the [100] dumbbell to be the lowest-energy configuration, in agreement with experimental data.[53] The non-split self-interstitial configuration in the octahedral position (O_h) turns out to be less favorable than the [100] dumbbell.

For large-angle grain boundaries our potentials predict higher energies in comparison with the VC potentials. This trend is illustrated in Tables I and II for the (111) twin and $\Sigma=5$ (210) and (310) [001] tilt boundaries. Another important quantity listed in the tables is the unstable stacking fault energy $\gamma_{\rm us}$. The meaning of this quantity is illustrated in Fig. 3, where we show $[\bar{2}11]$ sections of so-called γ surfaces[54,55] of Al and Ni on the (111) plane. A γ surface represents a plot of the planar fault energy γ as a function of the fault vector parallel to a certain crystalline plane. In our case, one half of the fcc crystal above a (111) plane was shifted rigidly with respect to the other half in the $[\bar{2}11]$ direction. The shift was implemented by small steps, and after each step the energy of the system was minimized with respect to atomic displacements normal to the (111) plane. Such displacements included both relative rigid-body translations of the two half-crystals and local atomic displacements in the [111] direction. The excess energy γ associated with the planar fault shows two local minima (Fig. 3): one at the perfect lattice position ($\gamma=0$) and the other at the shift vector $\frac{1}{6}[\bar{2}11]$ corresponding to the formation of an intrinsic stacking fault ($\gamma=\gamma_{\rm SF}$). The local maximum between the two minima represents an unstable configuration which is referred to as an ''unstable stacking fault.'' The unstable stacking fault energy $\gamma_{\rm us}$ determines the activation barrier for dislocation nucleation, and plays an important role in plastic deformation and fracture of metals.[56] The values of $\gamma_{\rm us}$ predicted by our potentials are notably higher than those predicted by the VC potentials, and are expected to be more realistic. Qualitatively, however, the behavior of γ along the shift direction $[\bar{2}11]$ is similar for all potentials considered here.

The surface energies predicted by our potentials came out to be higher than those predicted by the VC potentials. Both predictions, however, are generally on the lower side of the

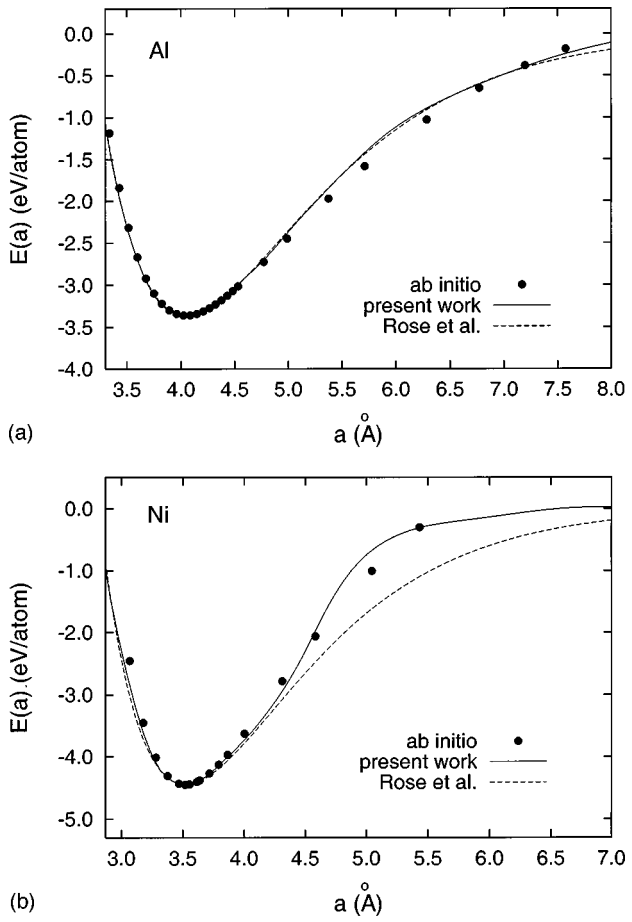

FIG. 4. Energy per atom of fcc Al (a) and fcc Ni (b) as a function of the lattice parameter. The *ab initio* values shown in this plot were subject to transformation according to Eq. (4). The empirical EOS of Rose *et al.* (Ref. 39) is shown for comparison.

experimental values[38] and the results of *ab initio* calculations (see, e.g., Ref. 57). As an additional check of this trend, we have evaluated here an unrelaxed value of $\gamma_s(111)$ for Al using an eight-layer supercell consisting of five (111) atomic layers and three (111) layers of vacuum. While the result of LAPW calculations was $\gamma_s(111)=974\,\mathrm{mJ/m^2}$, our potential and that of Voter and Chen gave 865 and 835 $\mathrm{mJ/m^2}$, respectively.

Historically, EAM potentials have been much more successful in accounting for the observed surface energies and surface relaxations and reconstructions than the previously used pair potentials. Nevertheless, EAM potentials are well known to underestimate surface energies consistently, the reasons probably being related to the large electron-density gradients occurring at the surface. The recognition of this fact was the reason why we assigned surface energies a low weight, and focused the attention on the properties of internal defects.

In Fig. 4 we show the equations of state of Al and Ni, calculated with our potentials, in comparison with the results of *ab initio* calculations and the empirical EOS of Rose *et al.*[39] The original *ab initio* energies were recalculated according to Eq. (4). For Al, the EAM-predicted EOS is very close to that of Rose *et al.*,[39] it is also consistent with the *ab initio* data, with some small deviations in the region of large expansions. For Ni, however, the *ab initio* energy values show a significant deviation from the empirical EOS toward higher energies in the expansion region. A remarkable feature of our potential for Ni is that it does predict a very similar deviation in the same region, and is in much better agreement with the *ab initio* values than the empirical EOS. This discrepancy is not very surprising, as the parameters for Rose's EOS were derived mainly from experimental data rather than *ab initio* calculations. Some results of *ab initio* calculations were used by Rose *et al.* for comparison. While these usually do follow a universal behavior, the *ab initio* values of E_0, R_0, and B often differ from the respective experimental data. We, therefore, need not expect our *ab initio* data to follow Rose *et al.*'s universal EOS exactly.

In Table IV we compare the *ab initio* structural energies of Al and Ni with those predicted by our potentials. This table represents the *ab initio* data set used at the testing stage, except for the values marked by the asterisk. The rms deviation obtained at the testing stage was 0.06 eV for Al and 0.15 eV for Ni. These values correspond to the saturation limit discussed in Sec. IV; they measure the limits of accuracy achievable in predicting the structural energies of Al and Ni in the framework of the EAM model. It should be emphasized, however, that these rms deviations were obtained by averaging over not only different structures but also different first-neighbor distances. More importantly, the accuracy in predicting the structural energies depends dramatically on the departure of the structures from equilibrium.

Indeed, Table IV shows that for the first-neighbor distance fixed at R_0 the agreement between the *ab initio* and EAM-predicted energies is very good. In this case the potentials successfully represent the right dependence of the energy on the local coordination in a wide range of different environments. The agreement also remains reasonably good under strong compression ($0.95R_0$) and even stronger expansion ($1.1R_0$), but the discrepancies increase drastically. The variation of R_0 is a very important test of the potentials, because the local atomic configurations arising in the core regions of crystalline defects may feature not only different ''abnormal'' coordinations but also distorted interatomic distances. It is noted that for Ni the strain gives rise to a larger discrepancy between *ab initio* and EAM-predicted energies than it does for Al. The latter feature is quite understandable: due to the higher bulk modulus of Ni, the same strain results in a larger increase in all structural energies of Ni in comparison with those of Al. Figure 5 illustrates all these features; it also demonstrates that the scatter of the data points is basically random, i.e., there is no noticeable systematic deviation between the structural energies predicted by the potentials and those obtained by *ab initio* calculations.

Table V summarizes the equilibrium first-neighbor distances and cohesive energies calculated for different alternative crystalline structures of Al and Ni using our potentials. They were obtained by minimizing the crystal energies with respect to a hydrostatic strain. The energies of noncubic structures were also minimized with respect to the c/a ratio. It should be emphasized that such constrained energy minimization does not guarantee that the structures obtained are truly stable or metastable. The calculation of the elastic constants of the structures reveals that some of them are elastically unstable. In Table V, the number of nearest neighbors in each structure, z, is also indicated. (Since the $A15$ struc-

TABLE IV. Energies per atom (in eV) of different crystalline structures of Al and Ni calculated by the LAPW method and by the present EAM potentials. Each structural energy is given for three first-neighbor distances: $0.95R_0$, R_0, and $1.1R_0$, where R_0 is the equilibrium first-neighbor distance in the fcc phase. The energies marked by the asterisk were fitted during the development of the EAM potentials, all other EAM-generated energies are predicted by the potentials. *Fit to the *ab initio* energy as part of the development of the potential.

		$0.95R_0$		R_0		$1.1R_0$	
Element	Structure	*ab initio*	EAM	*ab initio*	EAM	*ab initio*	EAM
Al	fcc	−3.25	−3.26	−3.36	−3.36*	−3.10	−3.07
	hcp[a]	−3.21	−3.24	−3.33	−3.33*	−3.09	−3.09
	bcc	−3.23	−3.24	−3.25	−3.24*	−2.93	−2.89
	sh[a]	−3.11	−3.04	−3.12	−3.10	−2.75	−2.84
	$L1_2$	−3.13	−3.05	−3.11	−3.02	−2.70	−2.66
	$A15$	−3.18	−3.19	−2.97	−2.89	−2.43	−2.33
	sc	−2.98	−2.96	−2.90	−2.92	−2.48	−2.58
	diamond	−2.52	−2.44	−2.36	−2.33*	−1.88	−1.96
Ni	fcc	−4.23	−4.28	−4.45	−4.45*	−3.95	−3.99
	hcp[a]	−3.20	−3.29	−4.42	−4.43*	−3.94	−4.00
	bcc	−4.23	−4.32	−4.30	−4.30*	−3.61	−3.74
	sh[a]	−3.99	−3.91	−3.90	−3.87	−3.20	−3.36
	$L1_2$	−3.84	−3.76	−3.75	−3.78	−3.01	−3.28
	sc	−3.66	−3.61	−3.44	−3.47	−2.66	−2.93
	diamond	−2.85	−2.56	−2.51	−2.50*	−1.73	−1.99

[a]With ideal c/a ratio.

ture includes two nonequivalent types of site, we give a value of z averaged over such sites.) As usual with the EAM model, the structures with lower coordination tend to be more compact (smaller R_0) and less stable (larger E_0). The $A15$ structure, however, demonstrates an exception to this rule, in that it turns out to be anomalously stable and has an unusually small R_0. For Al, the $A15$ structure is predicted to have the next-lowest energy after the fcc phase, and to be almost as stable as the hcp phase. For Ni, the $A15$ structure is slightly less stable than the hcp and bcc structures, but again considerably more stable than all other structures listed in the Table V. For Al, we have additionally calculated the energies of the $A15$ structure at ten different lattice parameters around the equilibrium by the LAPW method. The values $R_0 = 2.540$ Å and $E_0 = -3.28$ eV/atom evaluated from these data are in good agreement with our EAM predictions, and confirm the remarkable stability of this structure.

It is interesting to compare our cohesive energies of different structures of Ni with the results of recent total-energy tight-binding calculations.[58] In Table VI we make this comparison for those structures for which tight-binding cohesive energies are available. In addition to the structures considered previously, Table VI includes $A12$ (α-Mn), $A13$ (β-Mn), and $D0_3$ (Fe_3Al structure where Fe sites are occupied by Ni atoms while Al sites are vacant). For relatively simple structures, i.e., structures other than $A12$, $A13$, and $A15$, both types of calculation are consistent with the usual trend to greater stability (i.e., smaller E_0) of more compact structures (i.e., those with a larger coordination number z), as well as with the bond order concept (smaller energy per bond in more compact structures). There is good agreement between our energies and the tight-binding energies, although the latter show a tendency to some underbinding. In contrast, the cohesive energies obtained with the VC potential show considerable deviations from both previous data sets, with a noticeable tendency to overbinding. The ''exotic'' structures $A12$, $A13$, and $A15$ fall out of this trend, in that they show anomalously large stability. This behavior is consistent with the known fact that the number of first-neighbor ''bonds,'' z, is not always an adequate measure of compactness and stability of crystals, and that further neighbors should be also taken into account.

As a further test of transferability of our potentials to other, particularly noncubic, environments it was interesting to study the energy behavior along strong deformation paths. In Fig. 6 we show the energies of Al and Ni under a volume-conserving tetragonal strain along the so-called Bain path.[59] In the *ab initio* and EAM calculations the atomic volume was fixed at the equilibrium value Ω_0 predicted for the fcc phase by *ab initio* and EAM calculations, respectively. The minimum at $c/a = 1$ reflects the stability of the fcc phase, while the maximum observed at $c/a = 1/\sqrt{2}$ corresponds to a nonequilibrium bcc phase. Although our potentials and those of Voter and Chen predict qualitatively the same behavior of the energy, our potentials demonstrate much better agreement with *ab initio* results.

Figure 7 shows the calculated energy contour plot for Al along the Bain path, including both hydrostatic and tetragonal distortions. The bcc structure, relaxed with respect to its atomic volume Ω, corresponds to the saddle point in this plot. The elastic constants calculated for this structure satisfy the instability criterion $c_{11} < c_{12}$. These observations indicate that the bcc structure of Al is elastically unstable and, if allowed to evolve under the internal forces, it either returns to the ground-state fcc structure or develops some further tetragonal distortion and turns to a metastable body-centered

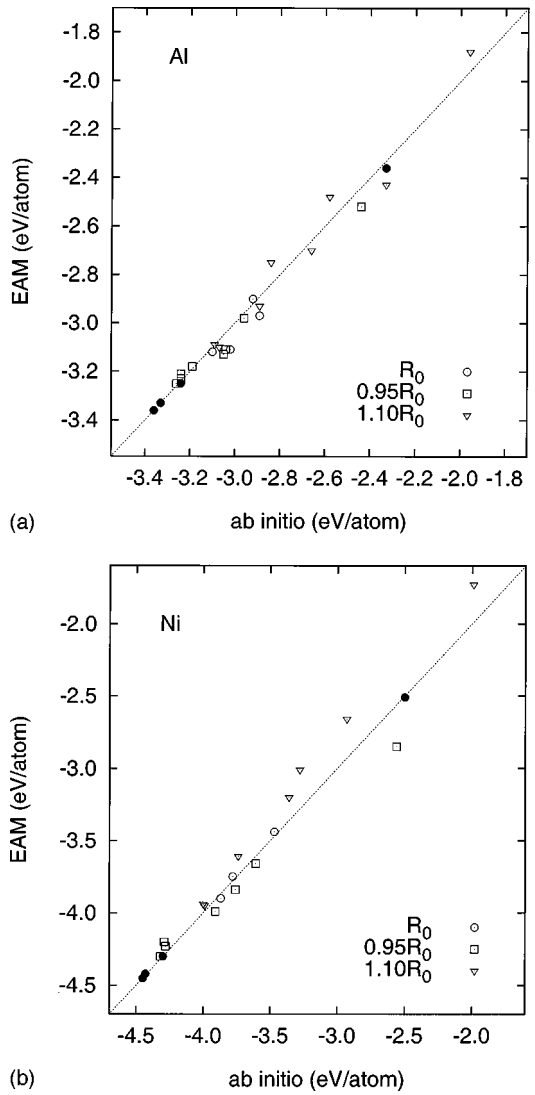

FIG. 5. Comparison of *ab initio* and EAM-predicted structural energies of Al (a) and Ni (b) for three fixed first-neighbor distances (see Table IV). The filled circles indicate the energies fitted as part of the development of the potentials; all other energies are predicted by the potentials. The line of perfect agreement (dotted line) is shown as a guide to the eye.

tetragonal (bct) structure. With reference to a bcc structure, the equilibrium c/a ratio of the bct structure equals 0.775, with a first-neighbor distance $R_0=2.774$ Å and a cohesive energy $E_0=-3.30$ eV/atom. Similar features are also observed for Ni, with the bcc structure being unstable and the bct structure with $R_0=2.426$ Å, $E_0=-4.34$ eV/atom, and $c/a=0.905$ being metastable. In view of the good agreement observed in Fig. 6, we can conclude that our predictions with regard to the instability of the bcc structures and metastability of the bct structures of Al and Ni are confirmed by the *ab initio* calculations. It is interesting to note that the equilibrium c/a ratios predicted for Al and Ni are close to and lie on the either side of the ideal ratio $c/a=\sqrt{2/3}\approx 0.816$ corresponding to an A_a (or, which is equivalent, $A6$) crystalline structure with $z=10$. The two known prototypes of this structure, α-Pa ($c/a\approx 0.82$) and β-Hg ($c/a\approx 0.71$), also show deviations from the ideal c/a ratio.

For Al, we also calculated the energy under a trigonal strain, again with the atomic volume fixed at the respective equilibrium values for the fcc phase. In this case the primitive translation vectors of the structure are

$$\mathbf{a}_1=(a,b,b),$$

$$\mathbf{a}_2=(b,a,b),$$

$$\mathbf{a}_3=(b,b,a),$$

where the angle θ between the vectors is given by

$$\cos\theta=\frac{(2a+b)b}{a^2+2b^2}.$$

We thus obtain a fcc lattice when $\theta=60°$, a sc lattice when $\theta=90°$, and a bcc lattice when $\theta=109.471°$. As in the previous case, the energies obtained with our potential are in very good quantitative agreement with *ab initio* energies. In contrast, the VC potential shows strong deviations from the *ab initio* data, especially for the angles around the *sc* structure. The fact that the energy attains a local maximum at $\theta=90°$ reflect the elastic shear instability of the *sc* structure with $c_{44}<0$. In the contour plot of the energy versus θ and Ω/Ω_0, which is not shown here, this structure corresponds to a saddle point.

Returning to Fig. 1, it is seen that the potentials show some wiggles, particularly in their tails. Moreover, the second derivatives of the potential functions, although continuous, show rapid changes around some points. These features typically accompany cubic-spline fitting, and generally may lead to unphysical anomalies of some properties. Although no anomalous behavior was ever found by the authors in any calculations reported here, the reader should be warned that further tests might, in principle, reveal some anomalies. The latter seems to be almost improbable while dealing with molecular static simulations, but the risk increases as one goes to quasiharmonic calculations at high temperatures or any other methods that rely on smooth behavior of higher derivatives.

TABLE V. Cohesive energies and equilibrium first-neighbor distances in different crystalline structures of Al and Ni, as predicted by the present EAM potentials.

		Al		Ni	
Structure	z	R_0 (Å)	E_0 (eV/atom)	R_0 (Å)	E_0 (eV/atom)
fcc	12	2.864	−3.36	2.489	−4.45
hcp	12	2.830[a]	−3.33	2.467[b]	−4.43
bcc	8	2.802	−3.25	2.413	−4.34
sh	8	2.852[c]	−3.10	2.341[d]	−3.94
$L1_2$	8	2.755	−3.06	2.429	−3.80
$A15$	7.5	2.573	−3.35	2.256	−4.30
sc	6	2.741	−2.96	2.347	−3.62
diamond	4	2.616	−2.47	2.372	−2.56

[a] $c/a=1.756$.
[b] $c/a=1.617$.
[c] $c/a=1.02$.
[d] $c/a=0.97$.

TABLE VI. Cohesive energies E_0 (in eV/atom) of different crystalline structures of Ni predicted by total-energy tight-binding calculations (TB) (Ref. 58), by the present EAM potential (EAM), and by the EAM potential of Voter and Chen (VC) (Ref. 9).

	Structure									
Method	fcc	hcp	bcc	$L1_2$	$D0_3$	sc	diamond	$A12$	$A13$	$A15$
TB	−4.45	−4.41	−4.34[a]	−3.79	−3.67	−3.42	−2.51	−4.35	−4.39	−4.25
EAM	−4.45	−4.43	−4.34	−3.80	−3.74	−3.62	−2.56	−4.31	−4.34	−4.30
VC	−4.45	−4.44	−4.37	−3.94	−3.88	−3.91	−2.97	−4.35	−4.36	−4.32

[a]Fitted to reproduce the results of *ab initio* calculations.

V. DISCUSSION AND SUMMARY

As we mentioned in Sec. I, interatomic potentials offer the only way to simulate large ensembles of atoms at present. While the first atomistic simulations of this kind were based on pair potentials, by the late 1980s they were almost completely replaced by many-body potentials of the EAM type.[2,3] The successes and limitations of such potentials have been recently discussed in Refs. 60 and 61. At present, there are a great number of EAM-type interatomic potentials available for different metals, alloys, and intermetallic compounds. Although the quality of such potentials varies widely, a typical potential reproduces some basic physical properties of the material (such as the lattice parameter, cohesive energy, elastic constants, and vacancy formation energy), but often fails to reproduce many other, also important properties, such as the vacancy migration energy, the stacking fault energy and so on. It should be clearly realized that the drawbacks of EAM potentials have two different sources.

(1) The intrinsic shortcomings of the EAM model. Although very successful in accounting for the nature of metallic bonding, this simple model is based on certain approximations, which make it insufficient in many situations.[60,61]

(2) The drawbacks of the traditional procedures for developing EAM potentials. Many such potentials are based on a small database of experimental properties and/or a small number of fitting parameters, not to mention the failure to use modern algorithms for multidimensional parametrization.

For the second reason, many EAM potentials are less accurate than they could be within the intrinsic limitations of the EAM model. The abundance of such potentials and their use in many atomistic simulations has resulted in some underappreciation of the EAM as such, and the appearance of the view that EAM potentials are only good for studying trends, but not for producing quantitative data.

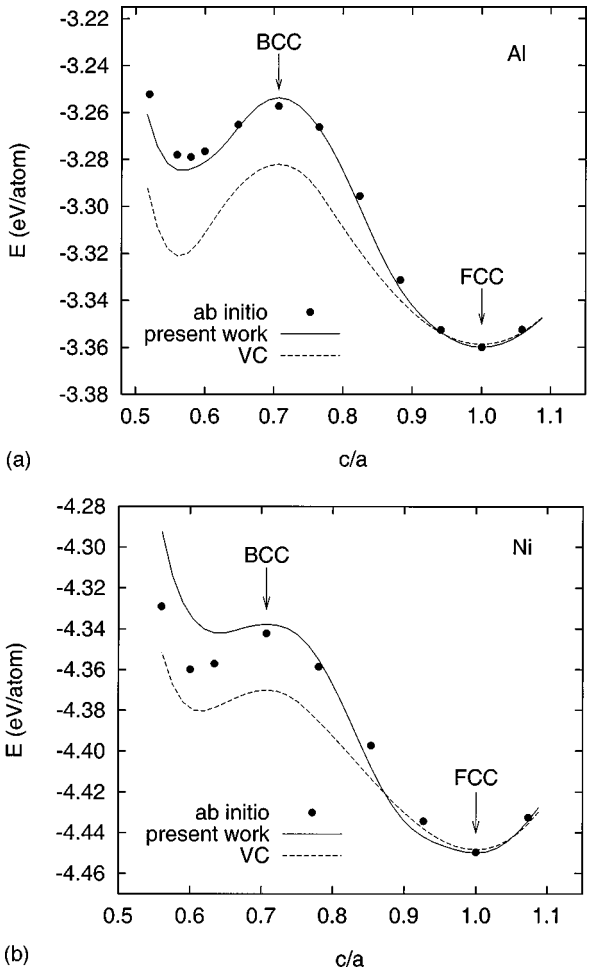

FIG. 6. Comparison of *ab initio* and EAM-predicted values of energy along the Bain path between the fcc and bcc structures of Al (a) and Ni (b). The calculations were performed with a fixed atomic volume corresponding to the equilibrium fcc phase.

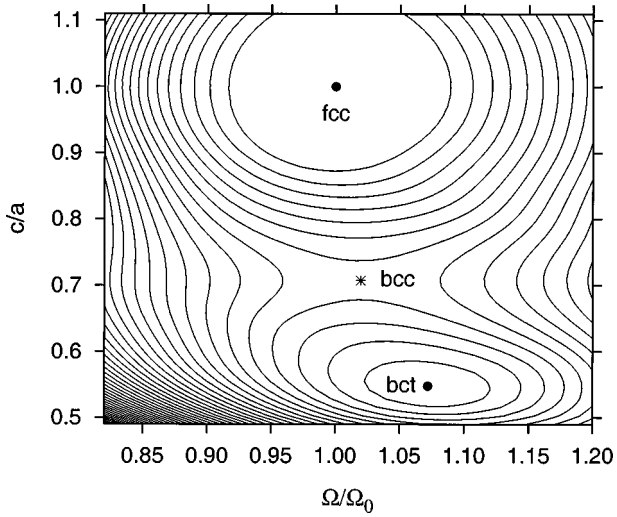

FIG. 7. The energy contours along the Bain path, calculated using our EAM potential for Al. The contours are shown in every 0.012 eV/atom. The saddle point (*) corresponds to the bcc structure, while the local minima (●) correspond to the stable fcc and metastable bct structures.

The chief objective of this paper was to demonstrate that one can increase the accuracy and reliability of EAM potentials dramatically by improving the procedures mentioned in point (2) above. In fact, due to such improvements one can eliminate almost all sources or error other than those dictated by the intrinsic limitations of the model. It then turns out that EAM potentials, at least for monoatomic metals, can reproduce many essential properties at a fairly good quantitative level. Moreover, within the region of configuration space sampled by the fitting database, EAM potentials are capable of predicting the energies of different configurations with an accuracy comparable with that of tight-binding or even *ab initio* calculations. The importance of such potentials cannot be overestimated. When an EAM potential is used in atomistic simulations, the computation time does not depend on the quality of the potential or the procedures by which it was generated. It therefore makes perfect sense to apply more elaborate fitting schemes and develop potentials that represent physical properties of the material more accurately and over a larger range of configurations.

The development of such potentials requires the use of a large data set including both experimental and *ab initio* data. Along with the traditional experimental quantities, the data set should include the vacancy migration energy, the stacking fault energy, a few short-wavelength phonon frequencies, and/or any other quantities for which reliable experimental information is available. It is suggested that the *ab initio* information be included in the form of the energies of different alternative crystalline structures, since such energies are very illustrative and can be conveniently generated using the supercell approach. The mismatch between the *ab initio* and experimental lattice periods can be taken care of by rescaling interatomic distances according to Eq. (4), but better approximations can also be developed in the future. The structural energies improve the transferability of the potential by sampling a large region of configuration space that is of interest in atomistic simulations but is not accessible by experimental measurements.

Another important improvement is the strategy of parametrization based on the alternation of fitting and testing steps.[6,10] The potential can be parametrized by fitting to the experimental data and part of the structural energies, while the other structural energies can be used for testing the potential. The rms deviation observed at the testing stage is the most meaningful criterion of quality of the potential. The optimum number of fitting parameters (N_p) for the chosen database can be found by starting with a small N_p and adding more parameters until the rms deviation of testing stops to decrease and reaches a saturation. The onset of the saturation indicates that the accuracy of the potential has approached the upper limit determined by the physical shortcomings of the EAM model. The potential corresponding to the onset of saturation is identified as the best potential for the given database.

As a demonstration of this approach we have constructed EAM potentials for Al and Ni. The *ab initio* part of the database included the energies of 6–7 different crystalline structures, each with three different nearest-neighbor distances, generated by LAPW calculations. The hcp, bcc, and diamond structural energies with the nearest-neighbor distance of the equilibrium fcc phase were included in the fitting database, while all other structural energies were used for testing the potentials. The potentials thus obtained represent the experimental values of the equilibrium and defect properties of Al and Ni with very good accuracy (Tables I and II), and even correctly reproduce the experimental phonon dispersion curves (Fig. 2). Moreover, the potentials also reproduce the right energies of different crystalline structures in a wide range of coordination numbers (Table III, Fig. 5). For Ni, our potential predicts almost the same cohesive energies of different crystalline structures as the recent total-energy tight-binding calculations[58] (Table VI). The energy behavior under tetragonal and trigonal strains, obtained by *ab initio* calculations, is also nicely reproduced by our potentials (Figs. 6 and 8). All these observations can be taken as a proof of good transferability of our potentials to various local environments encountered in atomistic simulations of lattice defects. Overall, it can be concluded that the potentials show excellent performance and predictive capacity at a *quantitative* level.

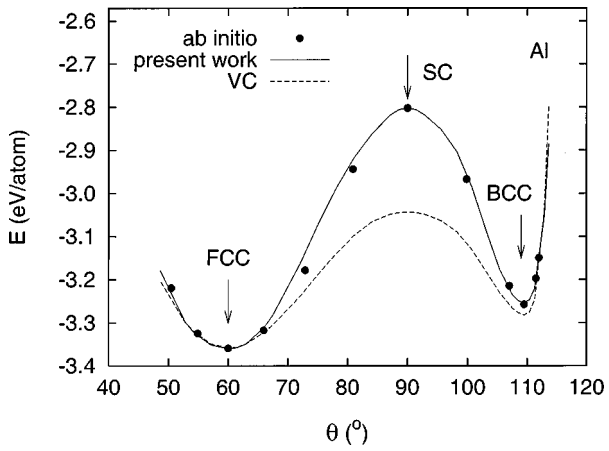

FIG. 8. Comparison of *ab initio* and EAM-predicted values of the energy per atom of Al under a trigonal strain. The trigonal angles θ corresponding to the fcc, bcc, and sc structures are indicated. The calculation was performed with a fixed atomic volume corresponding to the equilibrium fcc phase.

Different weights put on different properties take into account the strong and weak sides of the EAM,[60,61] and make our fitting scheme more flexible in constructing the best potential for a chosen spectrum of applications. The lowest weights are assigned to properties for which the experimental data are less reliable and/or which are represented by an EAM model less accurately due to its ''intrinsic shortcomings.'' In developing our potentials we gave a priority to bulk properties in contrast to surface energies. Because the EAM model is less accurate for the calculation of surface energies than for bulk properties, it is not very clear whether one potential can perform equally well for both. While this question calls for further studies, we chose here to construct our potentials with an emphasis on bulk properties and internal defects. In particular, since the potentials accurately reproduce the vacancy formation and migration energies, they can be good for simulations of diffusion phenomena. They also reproduce the experimental values of intrinsic stacking

fault energies and predict realistic unstable stacking fault energies, meaning that they are suitable for simulations of plastic deformation and fracture of Al and Ni. A prospective research topic is to study the behavior of dislocations under applied shear stresses, particularly to calculate the Peierls stress, using these potentials. Other interesting applications of these potentials include simulations of grain boundary structure, intergranular fracture, grain boundary sliding, grain boundary diffusion, and radiation damage of metals.

ACKNOWLEDGMENTS

This work was supported by the Office of Naval Research, U.S. Department of Defense, and the National Science Foundation (Grant No. DMR-9753243).

[1] M. S. Daw and M. I. Baskes, Phys. Rev. Lett. **50**, 1285 (1983).
[2] M. S. Daw and M. I. Baskes, Phys. Rev. B **29**, 6443 (1984).
[3] M. W. Finnis and J. E. Sinclair, Philos. Mag. A **50**, 45 (1984).
[4] F. Ercolessi, M. Parrinello, and E. Tosatti, Philos. Mag. A **58**, 213 (1988).
[5] F. Ercolessi and J. B. Adams, Europhys. Lett. **26**, 583 (1994).
[6] I. J. Robertson, V. Heine, and M. C. Payne, Phys. Rev. Lett. **70**, 1944 (1993).
[7] I. J. Robertson, D. I. Thomson, V. Heine, and M. C. Payne, J. Phys.: Condens. Matter **6**, 9963 (1994).
[8] S. M. Foiles, M. I. Baskes and M. S. Daw, Phys. Rev. B **33**, 7983 (1986).
[9] A. F. Voter and S. P. Chen, in *High temperature ordered intermetallic alloys*, edited by R. W. Siegel, J. R. Weertman, and R. Sundan, MRS Symposia Proceedings No. 82 (Materials Research Society, Pittsburgh, 1987), p. 175.
[10] M. C. Payne, I. J. Robertson, D. Thomson, and V. Heine, Philos. Mag. B **73**, 191 (1996).
[11] C. Kittel, *Introduction to Solid State Physics* (Wiley-Interscience, New York, 1986).
[12] *Handbook of Chemistry and Physics*, edited by R. C. Weast (CRC, Boca Raton, FL, 1984).
[13] *Metal Reference Book*, 5th ed, edited by C. J. Smith (Butterworth, London, 1976).
[14] G. Simons and H. Wang, *Single Crystal Elastic Constants and Calculated Aggregate Properties* (MIT Press, Cambridge, MA, 1977).
[15] H.-E. Schaefer, R. Gugelmeier, M. Schmolz, and A. Seeger, Mater. Sci. Forum **15-18**, 111 (1987).
[16] W. Wycisk and M. Feller-Kniepmeier, J. Nucl. Mater. **69&70**, 616 (1978).
[17] S. M. Foiles and M. S. Daw, J. Mater. Res. **2**, 5 (1987).
[18] D. J. Oh and R. A. Johnson, J. Mater. Res. **3**, 471 (1988).
[19] R. A. Johnson, Phys. Rev. B **39**, 12 554 (1989).
[20] R. G. Hoagland, M. S. Daw, S. M. Foiles, and M. I. Baskes, J. Mater. Res. **5**, 313 (1990).
[21] A. P. Sutton and J. Chen, Philos. Mag. Lett. **61**, 139 (1990).
[22] V. Vitek, G. J. Ackland and J. Cserti, in *Alloy Phase Stability Design*, edited by G. M. Stocks, O. P. Pope, and A. F. Giame MRS Symposia Proceedings No. 186 (Materials Research Society, Pittsburgh, 1991), p. 227.
[23] R. A. Johnson, J. Mater. Res. **7**, 883 (1992).
[24] S. Rubini and P. Ballone, Phys. Rev. B **48**, 99 (1993).
[25] C. L. Rohrer, Modell. Simul. Mater. Sci. Eng. **2**, 119 (1994).
[26] M. I. Baskes, J. E. Angelo and N. R. Moody, *Hydrogen Effect on Material Behaviour* (The Minerals, Metals and Materials Society, Warrendale, PA, 1995).
[27] M. I. Baskes, Acta Metall. Sin. **8**, 287 (1995).
[28] D. Farkas, B. Mutasa, C. Vailhe, and K. Ternes, Modell. Simul. Mater. Sci. Eng. **3**, 201 (1995).
[29] M. Ludwig and P. Gumbsch, Modell. Simul. Mater. Sci. Eng. **3**, 201 (1995).
[30] Y. Mishin and D. Farkas, Philos. Mag. A **75**, 169 (1997).
[31] R. W. Balluffi, J. Nucl. Mater. **69&70**, 240 (1978).
[32] L. E. Murr, *Interfacial Phenomena in Metals and Alloys* (Addison-Wesley, Reading, MA, 1975).
[33] R. Stedman and G. Nilsson, Phys. Rev. **145**, 492 (1966).
[34] R. J. Birgenau, J. Cordes, G. Dolling, and A. D. B. Woods, Phys. Rev. **136**, A1359 (1964).
[35] *Metals: Phonon States, Electron States, and Fermi Surfaces*, edited by K.-M. Hellwege and J. L. Olson, Landolt-Börnstein, New Series, Group III, Vol. 13, Pt. a (Springer, Berlin, 1981).
[36] Generally, the density at the jumping atom in the saddle-point configuration depends on the trade-off between fewer neighbors (due to the involvement of a vacancy), and shorter interatomic distances. Our calculations for Ni, Al, and a number of other metals using different EAM potentials available to us always show a lower density at the jumping atom in the relaxed saddle-point configuration than at a regular lattice site. The ratio of the two densities is typically around 0.8. This observation seems to be rather general, but at least it is true for Ni and Al.
[37] J. N. Murrell, Philos. Mag. A **73**, 163 (1996).
[38] W. R. Tyson and W. R. Miller, Surf. Sci. **62**, 267 (1977).
[39] J. H. Rose, J. R. Smith, F. Guinea, and J. Ferrante, Phys. Rev. B **29**, 2963 (1984).
[40] O. K. Andersen, Phys. Rev. B **12**, 3060 (1975).
[41] S. H. Wei and H. Krakauer, Phys. Rev. Lett. **55**, 1200 (1985).
[42] J. P. Perdew and Y. Wang, Phys. Rev. B **45**, 13 244 (1992).
[43] W. Kohn and L. J. Sham, Phys. Rev. **140**, A1133 (1965).
[44] H. J. Monkhorst and J. D. Pack, Phys. Rev. B **13**, 5188 (1976).
[45] M. J. Mehl, J. E. Osburn, and D. A. Papaconstantopoulos, Phys. Rev. B **41**, 10 311 (1990); **42**, 5362(E) (1991).
[46] M. J. Gillan, J. Phys.: Condens. Matter **1**, 689 (1989).
[47] F. Birch, J. Geophys. Res. **83**, 1257 (1978).
[48] R. A. Johnson, *Many Atom Interactions*, Proceedings in Physics, Vol. 48. Springer Verlag, Berlin (1990), p. 85.
[49] W. H. Press, S. A. Teukolsky, W. T. Vetterling, and B. P. Flannery, *Numerical Recipes in FORTRAN* (Cambridge University Press, Cambridge, 1992), p. 402.
[50] The potential function for Al and Ni $[V(r)$, $\rho(r)$, and $F(\overline{\rho})]$, and a postscript version of this paper are available, for retrieval via FTP over the WWW from http://cst-www.nrl.navy.mil/bind/eam.
[51] R. H. Rautioaho, Phys. Status Solidi B **112**, 83 (1982).
[52] K. H. Westmacott and R. L. Peck, Philos. Mag. **23**, 611 (1971).
[53] P. Ehrhart, J. Nucl. Mater. **69&70**, 200 (1978).
[54] V. Vitek, Philos. Mag. **73**, 773 (1968).
[55] V. Vitek, Cryst. Lattice Defects **5**, 1 (1974).

[56] J. R. Rice, J. Mech. Phys. Solids **40**, 239 (1992).
[57] S. B. Sinnott, M. S. Stave, T. J. Raeker, and A. E. DePristo, Phys. Rev. B **44**, 8927 (1991).
[58] M. J. Mehl and D. A. Papaconstantopoulos, Phys. Rev. B **54**, 4519 (1996).
[59] E. C. Bain, Trans. Am. Inst. Min. Metall. Pet. Eng. **70**, 25 (1924).
[60] A. F. Voter, *Intermetallic Compounds* (Wiley, New York, 1994), Vol. 1, Chap. 4, p. 77.
[61] G. J. Ackland, *The Encyclopedia of Advanced Materials* (Pergamon, Oxford, 1994), Vol. 1, p. 757.